Article

Day-Night imaging without Infrared Cutfilter removal based on metal-gradient perovskite single crystal photodetector

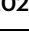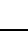Yao Ma[1,6], Leting Shan[2,6], Yiran Ying [3,6], Liang Shen[1,6], Yufeng Fu[2], Linfeng Fei[2], Yusheng Lei[4], Nailin Yue[5], Wei Zhang [5], Hong Zhang [4], Haitao Huang [3], Kai Yao [2] ✉ & Junhao Chu[4]

Day-Night imaging technology that obtains full-color and infrared images has great market demands for security monitoring and autonomous driving. The current mainstream solution relies on wide-spectrum silicon photodetectors combined with Infrared Cutfilter Removal, which increases complexity and failure rate. Here, we address these challenges by employing a perovskite photodetector based on Pb–Sn alloyed single crystal with a vertical bandgap-graded structure that presents variable-spectrum responses at different biases and extends the infrared detection range close to 1100 nm. Taking advantage of the Pb–Sn gradients in mobility and built-in field, the perovskite photo-detector shows a large linear dynamic range of 177 dB. In addition, the optoelectronic characteristics feature long-term operational stability over a year. We further develop an imaging module prototype without Infrared Cutfilter Removal that exhibits excellent color fidelity with RGB color differ-ences ranging from 0.48 to 2.46 under infrared interference and provides over 26-bit grayscale resolution in infrared imaging.

Day-Night imaging technology with a wide wavelength sensitivity range from visible to near-infrared band offers operators the choice to deliver true-color visible light images in the daytime or exhibit black-and-white infrared images at night. There has been a growing demand for Day-Night imaging applications such as security monitors, machine vision, and autonomous driving[1–3]. Conventional silicon image sensors with on-chip Bayer filters have infrared (IR) sensitivity, which causes diluted visible signals with the IR component and the loss of color resolution[4]. In this manner, the mainstream solution is realized by combining with a mechanically retractable Infrared Cutfilter Removal (ICR). Although this approach allows for the successful commerciali-zation of camera systems, the concern about the weight and

mechanical reliability of ICR devices dramatically limits their applica-tion for long-term use. Accordingly, realizing a robust Day-Night ima-ger without the mechanical ICR is highly desirable for lightweight and highly robust systems, such as drone or vehicle cameras. Optical algorithms have reported the removal of ICR but suffer from tradeoffs between spatial and color resolution[5]. In addition, conventional image sensors based on silicon photodetectors have a dynamic range of 60 to 80 dB, while automotive-grade image sensors require at least 140 dB for high-quality imaging applications[6].

To address these challenges, multispectral photodetectors with spectrally selective responses to visible and IR spectra stand out. The integration of individual photodetectors has been recently

[1]State Key Laboratory of Integrated Optoelectronics, College of Electronic Science and Engineering, International Center of Future Science, Jilin University, Changchun, China. [2]Institute of Photovoltaics, School of Physics and Materials Science, Nanchang University, Nanchang, China. [3]Department of Applied Physics, The Hong Kong Polytechnic University, Hung Hom, Kowloon, Hong Kong, China. [4]State Key Laboratory of Photovoltaic Science and Technology, Shanghai Frontiers Science Research Base of Intelligent Optoelectronics and Perception, Institute of Optoelectronics, Fudan University, Shanghai, China. [5]College of Materials Science and Engineering, Electron Microscopy Center, Jilin University, Changchun, China. [6]These authors contributed equally: Yao Ma, Leting Shan, Yiran Ying , Liang Shen. ✉e-mail: yaokai@ncu.edu.cn

reported to achieve multispectral detection[7,8], which needs well-designed device architectures to access separate materials. Complementary to the multisource approach, multiband or multimode photodetectors have been demonstrated by using organic[9], quantum-dot[10], and 2D materials[11] to construct vertical-stacked configurations. As an alternative to conventional semiconductors, metal halide perovskites have been extensively explored in recent decades for various applications, including photodetectors, lasers, light-emitting diodes, and photovoltaics[12–15]. Perovskite single crystals are perfect candidates for imaging applications due to their unique properties of high extinction coefficient, tunable direct bandgap, and excellent operational stability[16,17]. Nevertheless, the implementation of a perovskite single crystal photodetector for Day-Night imaging without ICR could still be challenging because of two major technological obstacles. We should first prepare a high-quality perovskite single crystal with a narrow bandgap (≤ 1.2 eV)[18], and then, on this basis, realize varying spectral responses. Although the excellent solution-processability of perovskite materials allows access to the preparation of composition gradients with tunable spectral responses[19–22], most bandgap-graded perovskite compositions relying on halide gradient (Cl, Br, and I) demonstrated a limited bandgap tunability in the visible region[23]. There is still a lack of study on the facile preparation of narrow-bandgap perovskite single crystals with gradient bandgaps.

In this work, we develop variable-spectrum responsive photodetectors based on narrow-band Pb-Sn alloyed perovskite single crystals with vertical bandgap gradients. Through a combination of material characteristics and theory calculations, we demonstrate the effect of oxygen exposure on compositional gradients and elucidate the specific role of interactions between Sn perovskite and oxygen. The metal alloyed perovskite photodetectors allow a bias-switchable spectral response from visible to near-infrared region (close to 1100 nm) for Day-Night imaging, thus simplifying the apparatus. The gradient distribution of Pb-Sn alloying brings the benefits of a high mobility and built-in electric field, enabling the perovskite photodetector to achieve a -3 dB cut-off frequency of 46.4 kHz and a linear dynamic range (LDR) of 177 dB. Moreover, the tin-enriched surface inhibits the formation of undercoordinated degradation centers, offering operational stability for up to one year. Finally, the color reproduction capabilities under infrared interference for the perovskite photodetector are comparable with those of a commercial silicon photodetector with ICR. The high gray-level resolution makes it more widely available in Day-Night vision applications.

Results

Design and preparation of perovskite single crystals

Alloying Pb and Sn in perovskite compositions is an effective approach to realizing low bandgaps (1.1–1.4 eV) that cannot be reached with pure Pb compositions[24,25]. Thus, the preparation of Pb–Sn alloyed perovskite with bandgap gradients should make it possible to realize a photodetector with broad and variable spectrum response simultaneously (Fig. 1a). Note that for the growth of high-quality single crystals, controlling the elements, including solute molecules, temperature, and solvent, within the optimal single-crystal-growth zone is critical to minimize the defect density[26,27]. Thus, we shift our attention to oxygen exposure due to well-known oxidation states in the Sn-based materials. To avoid the disturbance of solvent evaporation[28], we design a flow-through environmental chamber (FEC) system that uses gas exchange to realize oxygen diffusion and maintain the crystal growth rate (Fig. 1b). In the FEC system, the quantity of oxygen diffusion is highly dependent on the oxygen concentration of the outside atmosphere, which can be precisely controlled by adjusting the gas sources. Three different flows with low (1 ppm), middle (10 ppm), and high (100 ppm) oxygen concentrations have been used in this work.

Due to the attractive stability of methylammonium (MA)-free composition[29,30], we prepared Pb–Sn alloyed single-crystal using triple-cation, containing cesium (Cs), formamidinium (FA), and GA = guanidinium (GA), as previous work reported by our group[31]. The metal alloyed single-crystal with the compositions of $Cs_{0.1}FA_{0.87}GA_{0.03}Pb_{1-x}Sn_x(I_{0.95}Br_{0.05})_3$ (x = 0.2, 0.3, 0.4) in the growth solution are donated as $Pb_{0.8}Sn_{0.2}$, $Pb_{0.7}Sn_{0.3}$, and $Pb_{0.6}Sn_{0.4}$, respectively. Detailed growth methods are provided in Supplementary Fig. 1. We use inductively coupled plasma optical emission spectrometry (ICP-OES) to quantify the incorporation level of Sn in the final single crystals as a function of the feed ratio in the growth solution, as shown in Fig. 1c and Supplementary Table 1. Except for the Pb:Sn ratio, the composition ratios (Cs/FA/GA and I/Br) in the crystals are close to those in the feed solution (Supplementary Table 2), derived from the results of nuclear magnetic resonance spectroscopy and X-ray photoelectron spectroscopy (XPS) (Supplementary Figs. 2 and 3). We performed X-ray diffraction (XRD) measurements and found no signs of phase impurities[32]. The apparent shift of XRD peaks (Fig. 1d, Supplementary Figs. 4 and 5) from 13.93° to 14.08° is related to that the increasing incorporation of Sn ions leads to a shrinkage of the perovskite lattice (119 pm of Pb^{2+} > 110 pm of Sn^{2+})[22,33]. In addition, the absorbance spectra of Pb−Sn alloyed crystals exhibit a red-shift proportional to the feed ratio of Sn concentration (Fig. 1e). As expected, the MA-free Pb−Sn alloyed crystals all show satisfying thermal stability. (Supplementary Fig. 6).

Although a high Sn concentration in the solution increases the Sn ratio in the final single crystals, the concentration of Sn incorporated into the crystal is much lower than that of the growth solution. We then prepared $Pb_{0.7}Sn_{0.3}$ single crystals by tuning the O_2 concentrations of the surrounding atmosphere. The rise of O_2 exposure levels from 1 to 100 ppm causes an inconspicuous shift of diffraction angles in the XRD pattern (Fig. 1d and Supplementary Fig. 7), consistent with the substantially unchanged Sn content derived from ICP-OES results (Supplementary Fig. 8). Nevertheless, higher O_2 concentrations leads to a noticeable increase in the full width at half maximum (FWHM) of high-resolution X-ray rocking curve (Fig. 1f), indicating that the severe O_2 exposure cause crystalline disorder.

Compositional gradient of perovskite single crystals

Aside from the bulk crystal structure, we characterized the vertical composition of the $Pb_{0.7}Sn_{0.3}$ crystals prepared under different surrounding atmospheres by time-of-flight secondary ion mass spectroscopy (TOF-SIMS). In the positive mode, the cation element distributions are recorded as a function of etching depth from the upper surface to the deep interior (Supplementary Fig. 9). As shown in the zoomed-in profile (Fig. 2a), Pb signals of all the crystals exhibit a rise at the upper surface and then level off after the initial ramp-up over 100 nm into the interior. In contrast, the Sn signal has a reverse tendency that drops quickly at first and then gradually stabilizes. Moreover, the gradients for Pb−Sn composition at the top surface can be effectively tuned by the O_2 concentration of the surrounding atmosphere. Taking the depth profile of the Sn ion, for example, the signal intensity ratio of the upper surface (maximum) to bulk (minimum) increases from 3.9 of low O_2 concentration to 10.8 of high O_2 concentration.

The 3D images of Sn distribution over a wide depth range at different concentrations of O_2 exposure (Fig. 2b) offer more intuitionistic information. During the growth of the Pb−Sn alloyed perovskite crystal, more O_2 permeation prompted Sn enrichment at the upper surface. In contrast, the Pb distribution has the reverse profile. Notably, the uniform distributions of Cs and FA ions (Fig. 2c) reflect that the metal variation maintains the perovskite structure at the upper surface. In addition, the diffraction peaks of grazing-incidence X-ray diffraction (GIXRD) patterns show a clear shift toward small diffraction angles as the increasing incident angle (Supplementary Fig. 10), indicating the gradual lattice expansion. The lattice variation further supports the feature of Sn-rich near the top surface of the single

crystals prepared with the O_2-involved growth process. Furthermore, the small absorption shoulder with broad edge of the alloyed single crystal confirms a gradient evolution of the optical bandgap (inset of Fig. 1e and Supplementary Fig. 11). Thus, the composition changes lead to a gradually increasing bandgap from the top surface to the interior, which is consistent with the upward shift of energy level[22,32] (Supplementary Fig. 12). Unlike the upper surface, the less pronounced Sn enrichment at the bottom side (Supplementary Fig. 13) should be ascribed to the crystal growth direction. We further used spatially resolved Auger electron spectroscopy (AES) mapping to investigate the Pb−Sn distribution profile in the lateral direction. As shown in Supplementary Fig. 14, the surface AES mapping images revealed a uniform metal distribution horizontally.

To understand the effect of oxygen diffusion on Sn enrichment, we performed XPS measurements on the top surface of $Pb_{0.7}Sn_{0.3}$ crystals prepared with varied O_2 exposure (survey spectra in Supplementary Fig. 15). As the increase of O_2 concentrations, the boost of Sn $3d$ and O $1s$ peak intensity are keeping pace. As shown in Fig. 2d, the Sn $3d$ high-resolution spectra are deconvoluted into Sn^{2+} and Sn^{4+} peaks. The relative ratio of Sn^{4+} to Sn^{2+} species increases significantly as the concentration of O_2 in the atmosphere grows. In contrast, the feed ratio of Pb:Sn has little impact on Sn oxidation (Supplementary Fig. 16). Furthermore, we monitored the Sn $3d$ spectra at different depths using argon ion etching and

found a remarkable drop of Sn^{4+}/Sn^{2+} ratios from the top surface to the bulk (Supplementary Fig. 17). The positive correlation that existed between Sn oxidation and enrichment implies the decisive role of oxygen diffusion in vertically Pb−Sn compositional gradient.

As a thermodynamic driving force[30,34,35], the key to facilitating Pb substitution is to regulate the formation enthalpy (ΔH_f) of the Pb−Sn alloying structure (Fig. 2e). According to the density functional theory (DFT) calculations, the positive enthalpies of the alloying structure (direct channel) indicate that the kinetic transformation of the Pb−Sn alloyed phase is not a thermally driven process (Supplementary Fig. 18 and Supplementary Table 3), which explains the low-doping regime of Sn^{2+} ion in the compositions. The progressively replacing Pb^{2+} with Sn^{2+} by increasing the O_2 concentration can be rationalized by considering the presence of numerous defects at the surface[36,37]. Among various trap-terminated surfaces, iodide vacancies are dominated because iodide can be easily oxidized under heating by the oxygen dissolved in solution[38], as revealed by the noticeable iodide deficiency at the upper surface (Supplementary Fig. 19). We, therefore, proposed a vacancy-mediated strategy (Fig. 2f), in which oxygen occupy the sites of iodine vacancy before lead substitution[39]. Compared to the direct channel, the calculated enthalpy for Pb−Sn alloying through the O_2-incorporated pathway is notably decreased (Supplementary Fig. 20 and Supplementary Table 3). Furthermore, the displacement of two metal
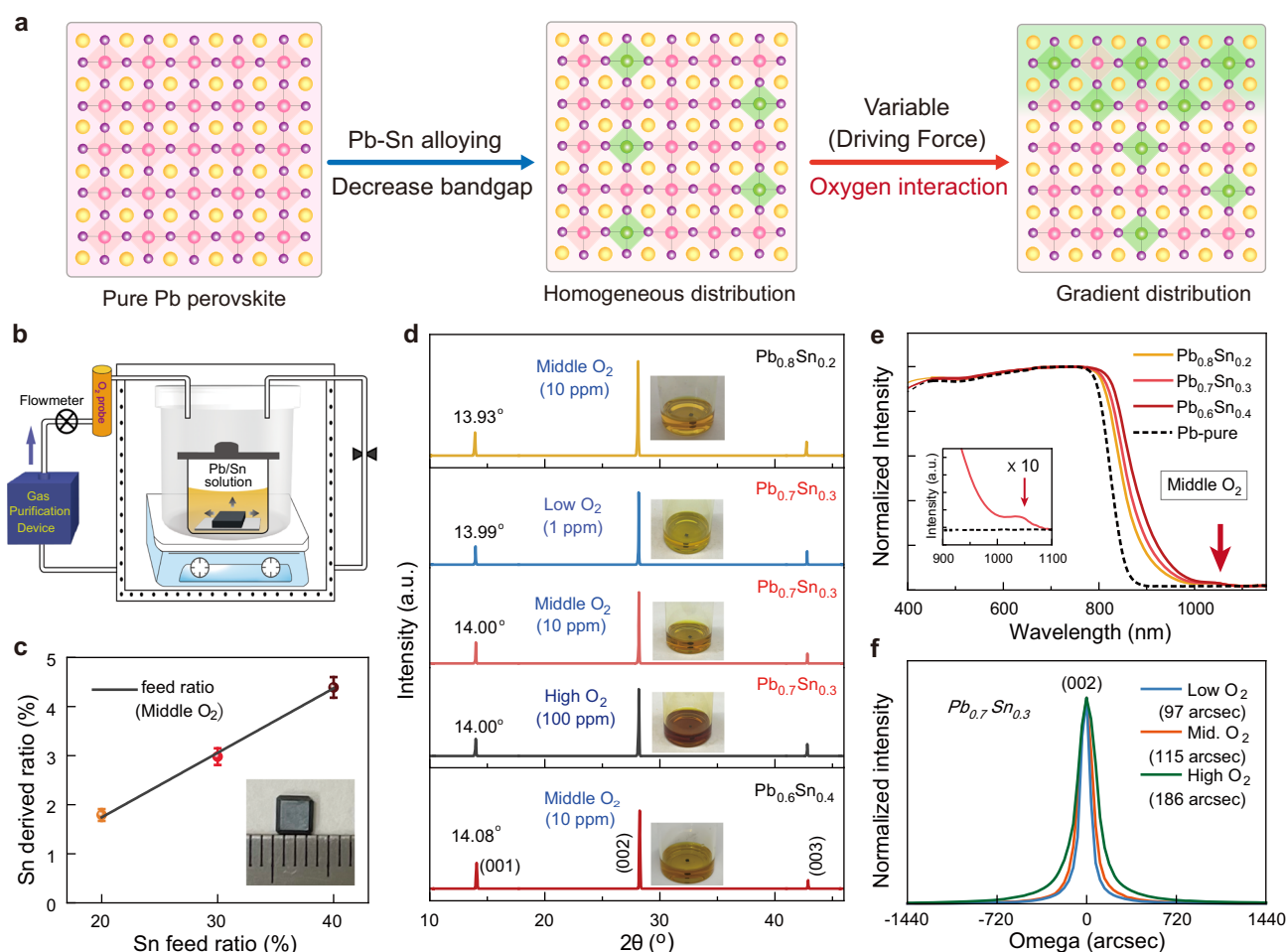

Fig. 1 | Growing process of Pb − Sn alloyed single crystals. a Schematics showing the Pb−Sn alloyed in homogenous and gradient structures. **b** Illustration of the FEC system to prepare Pb−Sn perovskite crystals under different surrounding atmospheres. **c** Derived [Sn]/([Sn]+[Pb]) atomic ratios from the ICP-OES as a function of the Sn concentration in the growth solution. The error bars are from experimental uncertainties. **d** X-ray 2θ scan on the top facet of Pb−Sn single crystals prepared under various Pb:Sn feed ratios and $Pb_{0.7}Sn_{0.3}$ single crystals prepared under various oxygen concentrations. The insets show the crystal growth solution. **e** Absorption spectra of Pb−Sn single crystals in reflectance mode. **f** High-resolution XRD rocking curve of the (002) diffraction peak of $Pb_{0.7}Sn_{0.3}$ single crystals prepared under different conditions.
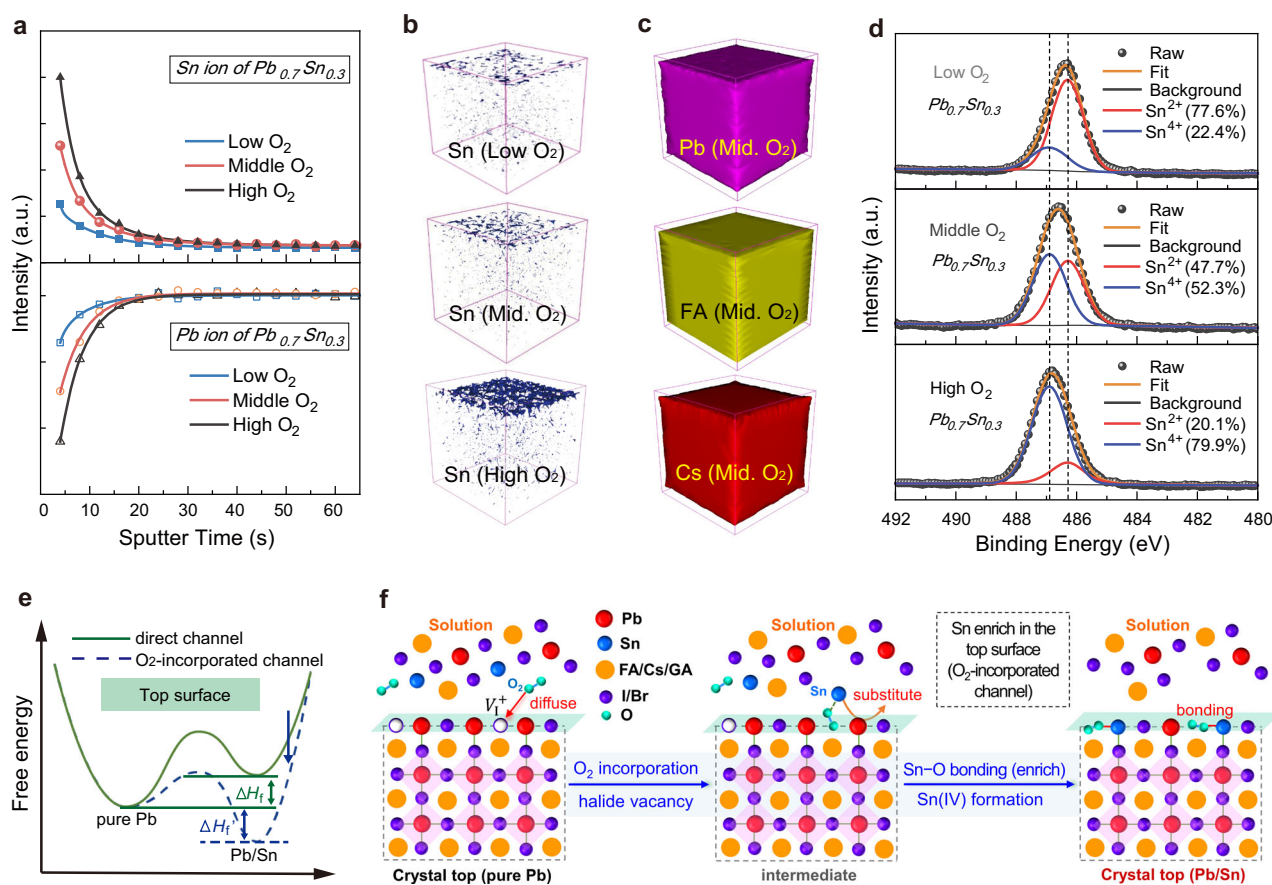
Fig. 2 | Vertical composition of Pb−Sn alloyed single crystals. a Enlarged TOF-SIMS depth profiling of Sn and Pb ions for various $Pb_{0.7}Sn_{0.3}$ single crystals in the upper surface region. The sputter rate is set to -8 nm/s. ToF-SIMS 3D tomography showing the distribution of Sn ions (**b**), Pb, FA, and Cs ions (**c**) for various $Pb_{0.7}Sn_{0.3}$ single crystals from the top surface to the 6 μm-deep inner bulk. Mid. is the abbreviation for middle. **d** XPS of Sn $3d$ core peaks performed on the top surface of $Pb_{0.7}Sn_{0.3}$ single crystals prepared under different surrounding atmospheres. **e** Ab initio energy diagram revealing the Pb−Sn alloying channels without (direct) and with O_2-incorporation. Note that the relative saddle point depth is undefined. **f** Schematic illustration of the Sn enrichment process at the top surface when oxygen diffuse into the iodine vacancies.

atoms in the supercell is thermodynamically favored by a negative ΔH_f, highlighting a tendency of Sn enrichment at the surface. In addition, the Bader charge analysis shows that O_2 in the incorporated channel gains electrons from tin (1.15 e)[40], which explains the severe oxidation of Sn^{2+} to Sn^{4+}.

For Sn-based perovskites, the spontaneous Sn oxidation that can be promoted at the surface by the Sn-poor environment (Sn vacancies) through a disproportionation reaction induces structural decomposition[41,42]. By comparison, we modified the vertical compositional distribution by providing an Sn-rich/I-poor condition near the upper surface and gradually transforming into a relatively moderate condition in the bulk. The calculated defect formation energy of V_{Sn}^{2-} for the O_2-incorporated structure shows an increase of 0.18 eV (Supplementary Fig. 21). Thus, the difficulty on migration of V_{Sn}^{2-} from the surface to the bulk region has been greatly increased, which effectively suppresses the formation of undercoordinated defects and the SnO_2 complex[43]. Besides, the interaction between Sn ions and oxygen in the perovskite lattice hinders further oxidation process at the crystal surface[39,44], ensuring its excellent environmental stability (Supplementary Fig. 22).

Photodetector with variable-spectrum response

To achieve variable-spectrum responsive photodetectors based on the vertical bandgap gradient Pb−Sn alloyed single crystal, we proposed a vertical photoconductive device with architecture as shown in Fig. 3a. Since the Pb−Sn alloyed perovskite can extend the absorption range to

the near-infrared band, the long-wavelength near-infrared (NIR) light is absorbed by the top surface of the perovskite crystals through the indium tin oxide (ITO) transparent electrode. At the same time, short-wavelength light can penetrate a deeper position to generate carriers. Under small bias voltage, the NIR light-generated carriers near the surface cannot drift across the entire crystal to the counter electrode (Ga). In contrast, visible light-generated carriers in bulk have a chance to be partially collected by the Ga electrode. When the bias voltage increases, the NIR light-generated carriers with longer drift lengths will contribute to the photocurrent. Therefore, we can utilize the variation of carrier drift distance with a bias voltage to control the response range of the photodetector.

We measured the external quantum efficiency (EQE) of the device under different bias voltages (Fig. 3b). Under a bias of −1 V, the detector shows a response peak around 800 nm with a cutoff edge around 880 nm, consistent with the pure Pb-based perovskite[31]. When the bias is increased to −3 V, the EQE spectra exhibit not only an improved intensity but also a second response peak around 940 nm, confirming a bias-regulated response range. In addition, the cutoff edge of the second response peak is close to 1100 nm, which is consistent with the absorption of Pb−Sn alloyed perovskite[45]. Afterward, we conducted a detailed analysis of the EQE response in the NIR region as a function of bias (Supplementary Fig. 23). The peak intensity was rapidly increased from around 5% (−1 V) to over 100% (−4.5 V). We further conducted a simulation on the simplified model of the photodetector using COMSOL Multiphysics software (Supplementary
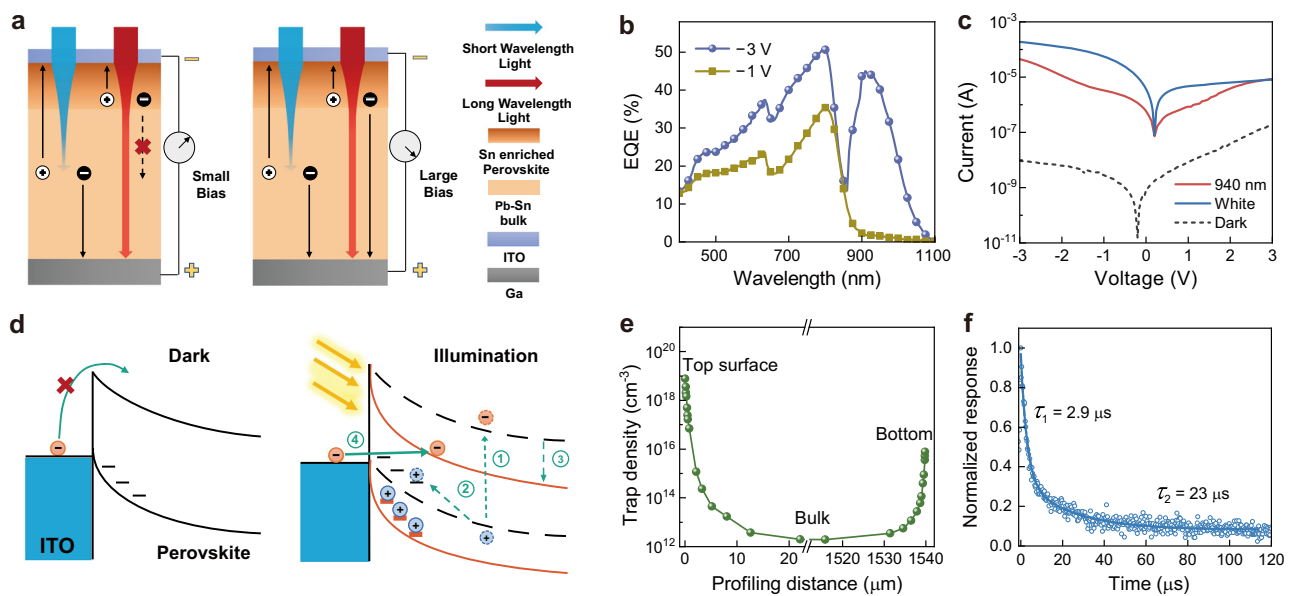
Fig. 3 | Mechanism of Pb−Sn alloyed single crystal photodetector. a Schematics of the mechanism of variable-spectrum responsive photodetectors under different biases. **b** EQE of the Pb−Sn perovskite photodetector under different biases. **c** Current-voltage curves of the perovskite photodetector under dark and (white and 940 nm light) illumination conditions. **d** Schematics of the energy band structure in the dark and under illumination. In the dark, the external electrons are blocked by the Schottky barrier, while the trap-induced charge injection mechanism under illumination can be divided into four steps: (1) electron-hole pair generation; (2) hole trapping process; (3) band bending and barrier narrowing; (4) electron tunneling process. **e** Density of trap states on the top and bottom surfaces of the crystal measured by DLCP. **f** The TPC spectra of the device, fitted by a second-order exponential function.

Fig. 24 and Supplementary Table 4). Under −1 V bias, the device produces almost no photocurrent under 940 nm light irradiation compared to the EQE under 750 nm light irradiation. With the bias voltage increasing, the EQE at 940 nm gradually rises, which is much higher than that of at 750 nm under −1 V. As a result, the ratio of EQE at 940 nm to EQE at 750 nm increases from approximately 0.02 under −1 V to approximately 0.85 under −3 V, in accordance with the measurement results.

The dark current of the device shows obvious rectification characteristics in the current-voltage curve (Fig. 3c), evidencing the formation of a Schottky junction. Furthermore, the EQE results under zero bias demonstrated the benefits of the Schottky junction on charge dynamics (Supplementary Fig. 25). Under illumination, the rectification characteristics of the device are reversed, showing negative voltage turn-on and positive voltage turn-off characteristics. Due to the best on-off ratio, the perovskite single crystals prepared under medium oxygen concentrations were used to assess the device performance in the following works (Supplementary Fig. 26). We also found that the photocurrent curve is influenced by the wavelength of light. As shown in the current-voltage curves on a linear scale (Supplementary Fig. 27), the threshold voltage depends on the illumination light, consistent with the simulation results (Supplementary Fig. 24c). The significantly boosting photocurrent under illumination indicates a trap-induced injection mechanism in the device[46], as illustrated in Fig. 3d. In the dark, the Schottky barrier between the ITO electrode and semiconductor blocks the injection of electrons from the cathode to the perovskite crystal. After illumination, the traps at the perovskite surface capture the photo-generated holes, thereby inducing the band bending with a thin Schottky barrier, which increases the probability of electron tunneling into the crystal. It is worth noting that the built-in electric field formed by the gradient junction accelerates the separation and transport of carriers (Supplementary Fig. 28).

To reveal the trap-induced carrier injection on the ITO side, we measured the trap concentration in the vertical distribution of the Pb−Sn perovskite crystal by the driver-level capacitance profile (DLCP). The spatial distribution of trap states (Fig. 3e) demonstrates that the trap concentration on the top surface (Sn enriched side) is three orders of magnitude higher than that on the bottom. As a comparison, the spatial distribution of trap states in pure Pb-based perovskite exhibited no significant difference in trap state concentration between the top and bottom sides (Supplementary Fig. 29), consistent with the results in the literature[37]. The contrast of trap density between the two sides is consistent with Sn oxidation and enrichment, which introduce defect energy levels near the valence band maximum (Supplementary Fig. 30). We used the space charge limited current technique to analyze the mobility and trap density based on electron- and hole-only devices (Supplementary Fig. 31). The derived mobility of holes (μ_h = 23.7 cm^2 V^{-1} s^{-1}) is much lower than that of electrons (μ_e = 293 cm^2 V^{-1} s^{-1}). We ascribed the impressive mobility to the intrinsic characteristics of Pb−Sn alloying[47,48]. We also conduct EQE measurements under positive bias, where holes need to cross the whole single crystal (Supplementary Fig. 32). Since the mobility of holes is much lower than that of electrons, long wavelength photo-generated carriers are more difficult to collect, and the EQE is therefore suppressed under negative voltage. Meanwhile, the measured electron and hole trap concentrations are 1.09×10^9 and 1.15×10^{10} cm^{-3}, respectively. We further used transient photocurrent (TPC) measurements to evaluate the carrier transport. The decay result matches well with a second-order exponential behavior (Fig. 3f), in which the slow order is attributed to the presence of trap carriers. Admittedly, traps can improve the response performance of the detector but partially deteriorate the response speed. The carrier dynamics variation under different bias voltages provides insight into the trap-induced carrier injection mechanism. As exhibited in Supplementary Fig. 33, the long-wavelength carriers are only generated in the surface tin-rich region, where the oxidized Sn^{4+} leads to severe non-radiative recombination, which will hinder electron collection under low bias voltage. Correspondingly, the lifetime of trapped holes is also significantly reduced by the trap-assisted recombination. In contrast, short-wavelength carriers generated in the bulk region of the crystal have a much longer lifetime due to the much lower defect density. Under high bias voltage, the drift distance of long-wavelength
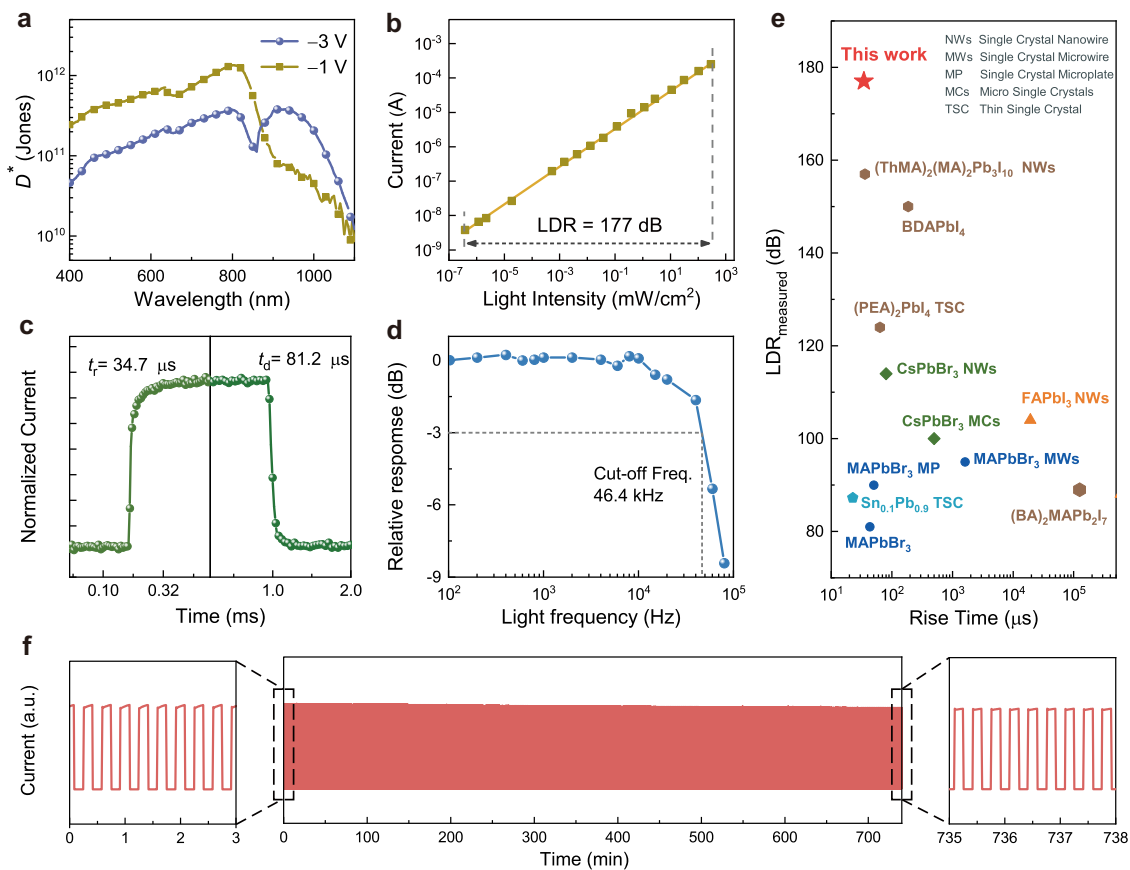
Fig. 4 | Characterizations of the Pb−Sn alloyed single crystal photodetector.
a Specific detectivity of the perovskite photodetector under different biases. **b** LDR of the perovskite photodetector measured at −1 V under 635 nm laser illumination with a slope of 0.56. **c** The response speed of the photodetector under white light. **d** The −3 dB cutoff frequency (abbreviated to Freq.) of the photodetector is 46.4 kHz, corresponding to the rise time. **e** Comparison of LDR and rise time performance of current photoconductive photodetectors based on perovskite single crystals with different colors representing various material compositions (refs. 58–68). **f** Continuous optical switching cycle stability test over 12 h, the left and right figures are the enlarged regions of the curve at the beginning and end of the test, respectively.

photo-generated carriers on the surface is enhanced, allowing electrons to drift out of the tin-rich region before recombination and then enter the bulk region with much lower defect density. After the effective collection of electrons, the lifetime of trapped holes is also significantly extended, resulting in effective trap-induced electron injection. Similarly, the carriers injected into the device can quickly drift out of the tin-rich region under high bias, showing the improvement of the collection efficiency.

Performance of the perovskite photodetector

The responsivity of the photodetector, calculated from the EQE results, reaches 0.23 A W⁻¹ at 800 nm under −1 V bias and 0.34 A W⁻¹ at 940 nm under −3 V bias (Supplementary Fig. 34). Based on the responsivity and noise current (Supplementary Fig. 35), we calculated the specific detectivity (D^*) to characterize the response performance under weak light conditions. As shown in Fig. 4a, the device exhibits a D^* of 1.3×10^{12} Jones at 800 nm and a negligible value at 940 nm under −1 V bias. Encouragingly, the D^* at 940 nm increases to 3.7×10^{11} Jones under −3 V bias, indicating that the detector also has great detection ability in the infrared band.

In imaging applications, the LDR of the photodetector determines the range of dark-to-bright tones that can be recorded in a given scene. Figure 4b exhibits that the photocurrent increased linearly under 635 nm illumination with the raising of the light intensity from around 3.6×10^{-7} to 360 mW cm⁻² for the Pb−Sn alloyed perovskite device, corresponding to a large LDR of 177 dB. In addition, the LDR measured at −3 V under 940 nm light irradiation is also >170 dB

(Supplementary Fig. 36). In particular, the generated photocurrent of the photodetector does not reach saturation even under the maximum light intensity. The improvement of LDR is mainly due to the reduction of internal defect density due to the high quality of the crystal, the increase of carrier mobility due to tin doping, and the promotion of carrier separation due to the built-in electric field introduced by tin gradient distribution[22,47,49]. The response speed of the photodetector is another important parameter from the aspect of practical applications. Herein, we have tested it under two working wavelengths. Under white light irradiation, the rise and fall time of the device are determined to be 34.7 and 81.2 μs, respectively (Fig. 4c). Under 940 nm infrared light irradiation, the rise time remains fairly static (31.9 μs), while the fall time is increased to 165 μs (Supplementary Fig. 37). The longer response time under NIR irradiation lies in two aspects that all NIR photo-generated carriers are located at the crystal top surface (higher trap density region) and need to travel through the entire crystal. In addition, we also described the frequency response characteristics of the detector to verify the response speed of the device. As displayed in Fig. 4d, the −3 dB cutoff frequency (f_{-3dB}) for the Pb−Sn detector is 46.4 kHz, in accordance with the rise time[50]. Considering the demand for fast speed and large LDR in imaging applications, the excellent performance is comparable to that of the state-of-the-art perovskite single crystal photoconductive detectors (Fig. 4e). The development of preparation methods by reducing the crystal thickness might further increase the device response speed.

The oxidation-induced degradation in the Sn-based device is a great challenge for their practical applications. We assessed the
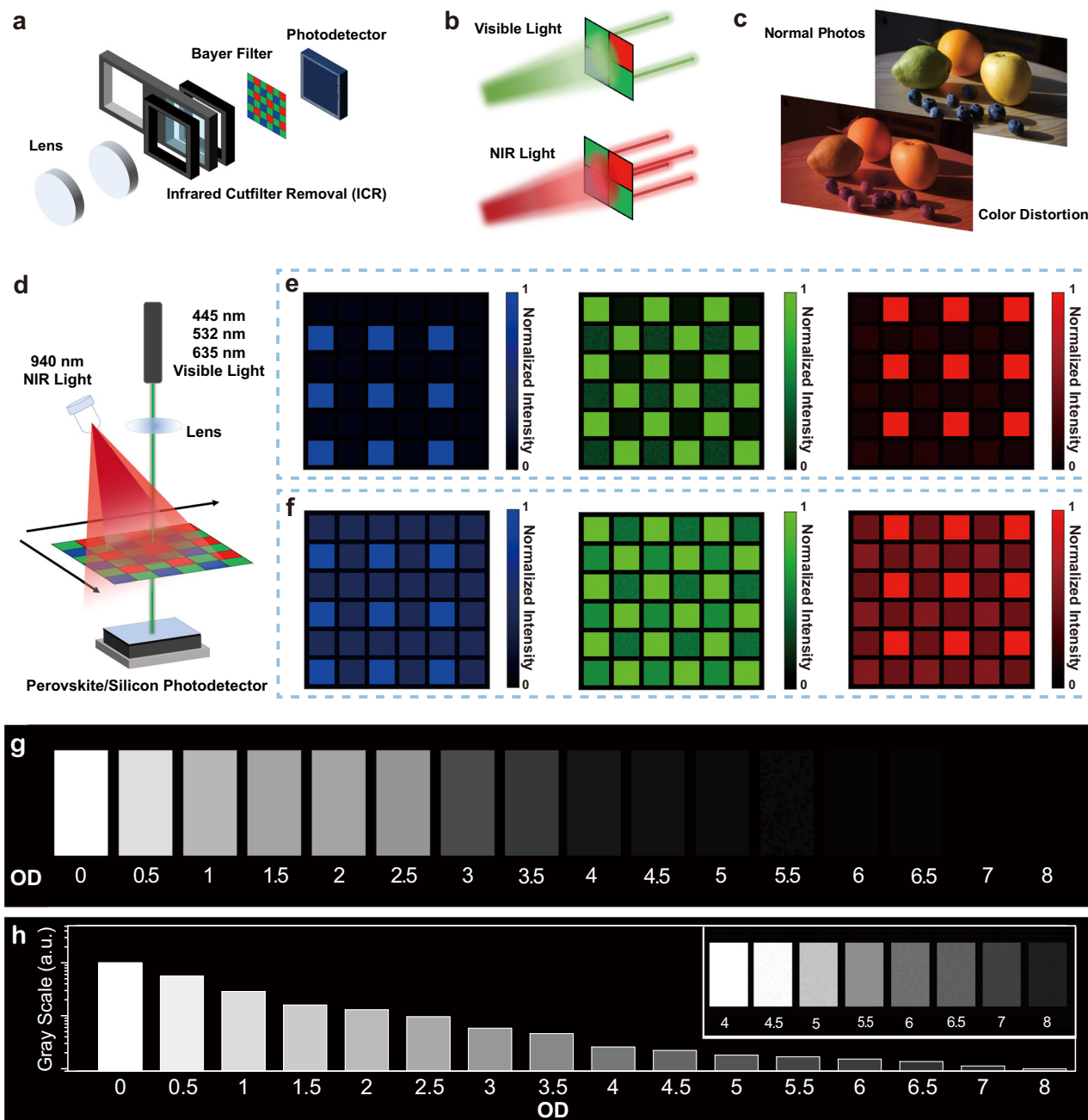
Fig. 5 | Demonstration of Day-Night imaging without ICR. a Schematic of the Day-Night camera using an ICR device. **b** Schematic of the selective transmission of Bayer filter for visible and infrared light. **c** The photos taken by the commercial camera with and without ICR, showing the color distortion caused by infrared interference. **d** Schematic of imaging equipment. Three colors of lasers are used as the target light, and 940 nm LEDs are used as interference light. Color reproduction ability of perovskite photodetectors (**e**) and Si photodetector (**f**). **g** Imaging results of a 16-step grayscale test chart. Below each step is the corresponding optical density (OD). 940 nm LEDs are used as the light source for the grayscale test. **h** The grayscale values corresponding to the imaging results. The inset shows the grayscale resolution of the grayscale test chart at low optical power after overexposure.

operational stability of unencapsulated Pb−Sn perovskite detectors in the air (Fig. 4f). The on-off switching characteristics exhibit a basically unchanged response under long-term continuous operation (12 h). Furthermore, we conducted a more intense shelf-life stability evaluation and found a constant on-off ratio in the device (Supplementary Fig. 38), retaining above 98% after one year.

Day-Night imaging without ICR

Finally, a prototype of an ICR-free imaging module based on the metal alloyed perovskite photodetector was demonstrated. The commercial Day-Night camera setup is mainly composed of a Si photodetector, Bayer filters, ICR, and lens[51] (Fig. 5a). As shown in Fig. 5b, the Bayer filter consists of different pixels that can selectively transmit three primary colors, i.e., red, green, and blue (RGB)[52], but all pixels are highly transparent to IR light[53] (Supplementary Fig. 39). Thus, Day-Night cameras need to switch IR-CUT filter during daylight to avoid unwanted color distortion in the photo image under IR interference (Fig. 5c). In contrast, the Pb−Sn alloyed perovskite photodetector makes the ICR-free possible with variable-spectrum responses, thus miniaturizing the apparatus. Moreover, our perovskite photodetector can switch between day and night imaging modes by adjusting the bias without mechanical switching devices prone to failure. To establish a match of

spectra region between the Bayer filter and the perovskite photodetector, we chose the low bias mode (−1 V) for full-color imaging in the daytime by filtering out light from 780 to 900 nm through low-cost notch filters. Meanwhile, we used the high bias mode (−3 V) for black-and-white imaging at night, since the second response peak at 940 nm is compatible with the widely used 940 nm complementary light (without red bursts).

A Bayer filter with commercial monochromatic filters was then employed to identify the color quality of the perovskite photodetector under infrared interference by comparison with commercial Si photodetector (Supplementary Fig. 39). We schematically obtained the color images from the photodetectors illuminated with a single monochromatic light (red: 650 nm, green: 532 nm, or blue: 445 nm) and IR complementary light (940 nm) (Fig. 5d). Unsurprisingly, the imaging results achieved by only using the Si photodetector present severe color distortion for all the monochromatic lights. In contrast, the perovskite photodetector maintains excellent color reproduction characteristics with no distinct distortion (Fig. 5e, f). In addition, the color reproduction ability of the perovskite photodetector reaches the level of the combination of Si photodetector with an IR-cut filter (Supplementary Fig. 40). It is worth noting that the weak response in blue pixels under 532 nm illumination is attributed to that the blue filter allows partial transmission for green light. Finally, based on the International Standard CIEDE2000 formula, we analyze the color difference (ΔE) of imaging results without algorithm optimization[54]. The smaller the ΔE, the better color fidelity is to the human eye. As summarized in Supplementary Table 5, the ΔE of perovskite photodetector increased from 0.48 for red to 2.46 for blue, which is much smaller that of silicon photodetector (34.65 for red and 34.41 for blue).

The figure of merits of Pb−Sn alloyed perovskite detector for IR imaging has also been experimentally studied by imaging the grayscale test card with 16 gray levels (density ranging from 0 to 8). The raw data in Fig. 5g shows the corresponding grayscale images recorded by the perovskite photodetector. Due to the greyscale limitation of the display medium, we could only differentiate gray levels with a density ranging from 0 to 6. Actually, the gray levels at low optical power were clearly distinguished by simply overexposing treatment (inset of Fig. 5h). The corresponding greyscale histogram (Fig. 5h) further demonstrates that the perovskite detector can provide over 26-bit resolution with the optical density value ranging from 0 to 8[55]. The perovskite detector with a large dynamic range ensures us to record broad brightness information from day to night, which is crucial in application scenarios such as nighttime light exposure and tunnel entry/exit[56].

Discussion

In summary, we have designed and studied variable-spectrum responsive photodetectors by developing perovskite single crystals with vertical metal gradients. Owing to the variation of carrier drift distance with bias, the composition-graded Pb−Sn alloying provides a bias-switchable spectral response for day and night imaging. We rationalize this compositional behavior by underscoring the decisive role of oxygen diffusion and illustrate the interactions between oxygen and tin perovskite. Metal alloyed perovskite single crystal detectors are shown to exhibit long-term stability beyond one year and high response performance, with an excellent D^* of 1.3×10^{12} Jones under −1 V bias, a large LDR of 177 dB, and a high −3 dB cut-off frequency of 46.4 kHz. The resulting color images produced by the perovskite photodetectors display excellent color reproduction performance, comparable with a commercial imager containing silicon photodetector and ICR. In addition, the 26-bit greyscale resolution highlights its broad application potential. We anticipate that the development of metal-alloyed perovskites opens an effective design strategy for transforming optoelectronic imaging technologies.

Methods

Crystal growth

All the series of Pb−Sn alloyed perovskite single crystals were grown using the inverse temperature crystallization (ITC) method[31]. Specifically, a stoichiometric molar ratio of $Cs_{0.1}FA_{0.87}GA_{0.03}Pb_{1-x}Sn_x(I_{0.95}Br_{0.05})_3$ ($x = 0.2$, 0.3, 0.4) precursor solution (1.0 M) was prepared by dissolving FAI, CsI, GAI, PbBr$_2$, PbI$_2$ and SnI$_2$ compounds in GBL (γ-butyrolactone). A tiny amount of benzylhydrazine hydrochloride (0.1 mM) was added into growth solutions as a reducing agent of starting materials[57]. Upon stirring for 12 h, the light-yellow color solutions were filtered through a 0.2 μm PTFE filter before being placed in a preheated (80 °C) oil bath of the FEC system. The solution was kept at 80 °C for 2 h, and then the temperature was gradually increased to 110 °C at a rate of 2 °C h^{-1}. Once the temperature rises, a gas mixture of nitrogen and oxygen with a flowing rate of 0.01 m^3 h^{-1} through the chamber. The oxygen concentration in the gas was adjusted from 1 ppm to 100 ppm. Finally, crystals approximately 3–5 mm in size were collected and stored under atmospheric conditions in the dark. Except for the composition of Pb: Sn ratio and oxygen concentration, all the Pb−Sn alloyed crystals are fabricated under similar conditions.

Characterization

XPS analysis was collected using a Thermo Scientific K-Alpha X-ray Photoelectron Spectrometer. The XRD spectra of the crystals were obtained using a high-resolution XRD (Rigaku SmartLab) equipped with Cu Kα radiation and a HyPix−3000 2D hybrid pixel array detector. The XRD patterns of the crystal powder were measured using a D8 Advance diffractometer from Bruker with a Cu Kα radiation source. The photocurrents are characterized by using a group of white LEDs with a light intensity of about 18 mW cm^{-2} as a white light source and 940 nm LEDs with a light intensity of about 15 mW cm^{-2} as an infrared light source. The external quantum efficiencies were measured by a Crowntech Q test Station 1000 AD measurement system.

Device fabrication

The front electrode was prepared by sputtering ITO (80 nm) on the top surface of the single crystals. The solidification of liquid gallium at the bottom served as an anode. For hole-only devices, gold electrodes were deposited by thermal evaporation on the upper and lower surfaces with a thickness of 100 nm. For electron-only devices, 20 nm thick C$_{60}$ and 100 nm thick copper electrodes were deposited sequentially on both sides.

DLCP measurements

For both Pb and Pb−Sn alloyed perovskites, the thicknesses of the crystal were measured first. Then, the crystal was cut transversely from the middle, dividing it into two parts: the upper and lower surfaces. The profile was polished with sandpaper of different roughness, after which the device with Cu/C$_{60}$/Perovskite/C$_{60}$/Cu structure was fabricated. Using the DLCP preset of the Keithley 4200 semiconductor parameter analyzer, the spatial distribution of trap states on the upper and lower surfaces was tested respectively, and then the DLCP data map was reduced according to the crystal thickness.

LDR measurements

Using 635 nm and 940 nm lasers as light sources with constant power, we adjusted the irradiation light intensity on the device by adding different neutral density filters in the optical path. A wide range of optical power adjustments can be achieved by combining filters with different ODs of 0.5, 1, 3, and 4. After adjusting the filter combination, the actual irradiation light intensity was further checked using the Newport 843-R optical power meter and the Newport 918D photodiode sensor. Keysight B2901A sourcemeter was used to record the

photocurrent of the photodetector. The photodetector operated at −3 V and −1 V bias when tested at 940 and 635 nm, respectively.

Imaging
Bayer filter is made of commercial monochromatic filters for three primary colors. When the laser was irradiated onto the device through the corresponding wavelength filter, the generated photocurrent of the device was calibrated to 255. Meanwhile, the dark current of the device was calibrated to 0. Using 445, 532, and 635 nm lasers as light sources, the color images were obtained by current inversion after scanning the whole Bayer filter. Commercial silicon detectors performed the same imaging process as perovskite photodetectors. By contrast, a 650 nm infrared cutoff filter was placed in front of the silicon detector as a demonstration of normal camera imaging results.

Gray scale test chart imaging
After laser cutting the mold, a grayscale test chart with 16 steps was assembled by using a group of reflective neutral density filters. Then, using 940 nm LEDs as a light source, imaging was performed in the same process described above after focusing through the objective lens.

Data availability
The main data generated in this study are provided in the Supplementary Information/Source Data file. Additional data that support the findings of this work are available from the corresponding authors upon request. Source data are provided with this paper.

References
1. Almalioglu, Y. et al. Deep learning-based robust positioning for all-weather autonomous driving. *Nat. Mach. Intell.* **4**, 749–760 (2022).
2. Zaidi, S. S. A. et al. A survey of modern deep learning based object detection models. *Digit Signal Process.* **126**, 103514 (2022).
3. Chen, L. et al. Milestones in autonomous driving and intelligent vehicles: survey of surveys. *IEEE Trans. Intell. Veh.* **8**, 1046–1056 (2023).
4. Song, Y. M. et al. Digital cameras with designs inspired by the arthropod eye. *Nature* **497**, 95–99 (2013).
5. Enge, A. D. & DiBella, J. A. Accurate color with increased sensitivity using IR. *SPIE Proc.* **8298**, 236–243 (2012).
6. Takayanagi, I. & Kuroda, R. HDR CMOS image sensors for automotive applications. *IEEE Trans. Electron Devices* **69**, 2815–2823 (2022).
7. Yuan, S., Naveh, D., Watanabe, K., Taniguchi, T. & Xia, F. A wavelength-scale black phosphorus spectrometer. *Nat. Photon.* **15**, 601–607 (2021).
8. Wang, V., Uddin, S. Z., Park, J. & Javey, A. Highly multicolored light-emitting arrays for compressive spectroscopy. *Sci. Adv.* **9**, eadg1607 (2023).
9. Lan, Z. et al. Near-infrared and visible light dual-mode organic photodetectors. *Sci. Adv.* **6**, eaaw8065 (2020).
10. Tang, X., Ackerman, M. M., Chen, M. & Guyot-Sionnest, P. Dual-band infrared imaging using stacked colloidal quantum dot photodiodes. *Nat. Photon.* **13**, 277–282 (2019).
11. Hwang, A. et al. Visible and infrared dual-band imaging via Ge/MoS$_2$ van der Waals heterostructure. *Sci. Adv.* **7**, eabj2521 (2021).
12. Zhou, Y. et al. Self-powered perovskite photon-counting detectors. *Nature* **616**, 712–718 (2023).
13. Kim, J. S. et al. Ultra-bright, efficient and stable perovskite light-emitting diodes. *Nature* **611**, 688–694 (2022).
14. He, Y., Hadar, I. & Kanatzidis, M. G. Detecting ionizing radiation using halide perovskite semiconductors processed through solution and alternative methods. *Nat. Photon.* **16**, 14–26 (2022).
15. Qin, C. et al. Stable room-temperature continuous-wave lasing in quasi-2D perovskite films. *Nature* **585**, 53–57 (2020).
16. Sakhatskyi, K. et al. Stable perovskite single-crystal X-ray imaging detectors with single-photon sensitivity. *Nat. Photon.* **17**, 510–517 (2023).
17. Yu, W. et al. Single crystal hybrid perovskite field-effect transistors. *Nat. Commun.* **9**, 5354 (2018).
18. Morteza Najarian, A. et al. Sub-millimetre light detection and ranging using perovskites. *Nat. Electron.* **5**, 511–518 (2022).
19. Zuo, C. et al. Perovskite films with gradient bandgap for self-powered multiband photodetectors and spectrometers. *Nano Res.* **16**, 10256–10262 (2023).
20. Zhang, M.-N. et al. Spectrum projection with a bandgap-gradient perovskite cell for colour perception. *Light Sci. Appl.* **9**, 162 (2020).
21. Gu, F. et al. Spatial bandgap engineering along single alloy nanowires. *J. Am. Chem. Soc.* **133**, 2037–2039 (2011).
22. Lei, Y. et al. A fabrication process for flexible single-crystal perovskite devices. *Nature* **583**, 790–795 (2020).
23. Wang, X. et al. Solution-processed halide Perovskite single crystals with intrinsic compositional gradients for X-ray detection. *Chem. Mater.* **32**, 4973–4983 (2020).
24. Eperon, G. E. et al. Perovskite-perovskite tandem photovoltaics with optimized band gaps. *Science* **354**, 861–865 (2016).
25. Dey, K., Roose, B. & Stranks, S. D. Optoelectronic properties of low-bandgap halide perovskites for solar cell applications. *Adv. Mater.* **33**, 2102300 (2021).
26. Dunlap-Shohl, W. A., Zhou, Y., Padture, N. P. & Mitzi, D. B. Synthetic approaches for halide perovskite thin films. *Chem. Rev.* **119**, 3193–3295 (2019).
27. Liu, Y. et al. Low-temperature-gradient crystallization for multi-inch high-quality perovskite single crystals for record performance photodetectors. *Mater. Today* **22**, 67–75 (2019).
28. Jia, B. et al. Airflow-controlled crystallization for a multi-Inch 2D halide perovskite single-crystal scintillator for fast high-resolution X-ray imaging. *ACS Energy Lett.* **8**, 590–599 (2023).
29. Turren-Cruz, S.-H., Hagfeldt, A. & Saliba, M. Methylammonium-free, high-performance, and stable perovskite solar cells on a planar architecture. *Science* **362**, 449–453 (2018).
30. Bu, T. et al. Lead halide–templated crystallization of methylamine-free perovskite for efficient photovoltaic modules. *Science* **372**, 1327–1332 (2021).
31. Jiang, J. et al. Synergistic strain engineering of perovskite single crystals for highly stable and sensitive X-ray detectors with low-bias imaging and monitoring. *Nat. Photon.* **16**, 575–581 (2022).
32. Cao, J. et al. High-performance Tin–Lead mixed-perovskite solar cells with vertical compositional gradient. *Adv. Mater.* **34**, 2107729 (2022).
33. Chen, Q. et al. Under the spotlight: the organic–inorganic hybrid halide perovskite for optoelectronic applications. *Nano Today* **10**, 355–396 (2015).
34. Liu, X. et al. Stabilization of photoactive phases for perovskite photovoltaics. *Nat. Rev. Chem.* **7**, 462–479 (2023).
35. Chen, T. et al. Entropy-driven structural transition and kinetic trapping in formamidinium lead iodide perovskite. *Sci. Adv.* **2**, e1601650 (2016).
36. Xue, J., Wang, R. & Yang, Y. The surface of halide perovskites from nano to bulk. *Nat. Rev. Mater.* **5**, 809–827 (2020).
37. Ni, Z. et al. Resolving spatial and energetic distributions of trap states in metal halide perovskite solar cells. *Science* **367**, 1352–1358 (2020).
38. Liu, Y. et al. Inch-sized high-quality perovskite single crystals by suppressing phase segregation for light-powered integrated circuits. *Sci. Adv.* **7**, eabc8844 (2021).
39. Ju, Y. et al. The evolution of photoluminescence properties of PEA$_2$SnI$_4$ upon oxygen exposure: insight into concentration effects. *Adv. Funct. Mater.* **32**, 2108296 (2022).

40. Zhang, Z. et al. Revealing superoxide-induced degradation in lead-free tin perovskite solar cells. *Energy Environ. Sci.* **15**, 5274–5283 (2022).

41. Ricciarelli, D., Meggiolaro, D., Ambrosio, F. & De Angelis, F. Instability of Tin Iodide Perovskites: Bulk p-Doping versus surface Tin oxidation. *ACS Energy Lett.* **5**, 2787–2795 (2020).

42. Meggiolaro, D., Ricciarelli, D., Alasmari, A. A., Alasmary, F. A. S. & De Angelis, F. Tin versus lead redox chemistry modulates charge trapping and self-doping in Tin/Lead Iodide Perovskites. *J. Phys. Chem. Lett.* **11**, 3546–3556 (2020).

43. Kim, E. H., Lee, J. H., Kim, S. H., Gu, J. H. & Lee, D. A-site effect on the oxidation process of Sn-halide perovskite: first-principles calculations. *J. Phys. Chem. Lett.* **12**, 9691–9696 (2021).

44. Lanzetta, L. et al. Degradation mechanism of hybrid tin-based perovskite solar cells and the critical role of tin (IV) iodide. *Nat. Commun.* **12**, 2853 (2021).

45. Zhao, Y., Li, C., Jiang, J., Wang, B. & Shen, L. Sensitive and stable Tin–Lead hybrid perovskite photodetectors enabled by double-sided surface passivation for infrared upconversion detection. *Small* **16**, 2001534 (2020).

46. Shen, L., Fang, Y., Wei, H., Yuan, Y. & Huang, J. A highly sensitive narrowband nanocomposite photodetector with gain. *Adv. Mater.* **28**, 2043–2048 (2016).

47. Senanayak, S. P. et al. Charge transport in mixed metal halide perovskite semiconductors. *Nat. Mater.* **22**, 216–224 (2023).

48. Liu, A. et al. High-performance inorganic metal halide perovskite transistors. *Nat. Electron.* **5**, 78–83 (2022).

49. Shi, D. et al. Low trap-state density and long carrier diffusion in organolead trihalide perovskite single crystals. *Science* **347**, 519–522 (2015).

50. Wei, H. et al. Sensitive X-ray detectors made of methylammonium lead tribromide perovskite single crystals. *Nat. Photon.* **10**, 333–339 (2016).

51. Koyama, S., Inaba, Y., Kasano, M. & Murata, T. A Day and Night Vision MOS imager with robust photonic-crystal-based RGB-and-IR. *IEEE Trans. Electron Device* **55**, 754–759 (2008).

52. Hou, Y. et al. Retina-inspired narrowband perovskite sensor array for panchromatic imaging. *Sci. Adv.* **9**, eade2338 (2023).

53. Hertel, D., Marechal, H., Tefera, D. A., Fan, W. & Hicks, R. A low-cost VIS-NIR true color night vision video system based on a wide dynamic range CMOS imager. In *2009 IEEE Intelligent Vehicles Symposium*, 273–278 (2009).

54. International Commission on Illumination. ISO/CIE 11664-6:2014 Colorimetry-Part 6: CIEDE2000 Colour-difference formula.

55. Wan, P., Tan, J., Lian, X. & Ji, X. High bit-depth image acquisition framework using embedded quantization bias. *IEEE Trans. Comput. Imaging* **5**, 556–569 (2019).

56. Mertens, T., Kautz, J. & Van Reeth, F. Exposure fusion: a simple and practical alternative to high dynamic range photography. *Comput. Graph. Forum* **28**, 161–171 (2009).

57. Chen, S., Xiao, X., Gu, H. & Huang, J. Iodine reduction for reproducible and high-performance perovskite solar cells and modules. *Sci. Adv.* **7**, eabe8130 (2021).

58. Chang, Z. et al. Narrow-bandgap Sn–Pb mixed perovskite single crystals for high-performance near-infrared photodetectors. *Nanoscale* **15**, 5053–5062 (2023).

59. Malo, T. A. et al. Suppressing the multiple nucleation for the uniform growth of perovskite single-crystal microplates arrays toward high-performance optoelectronic devices. *Adv. Funct. Mater.* **32**, 2209563 (2022).

60. Gu, L. et al. A biomimetic eye with a hemispherical perovskite nanowire array retina. *Nature* **581**, 278–282 (2020).

61. Deng, W. et al. Aligned single-crystalline perovskite microwire arrays for high-performance flexible image sensors with long-term stability. *Adv. Mater.* **28**, 2201–2208 (2016).

62. Li, J. et al. Self-trapped state enabled filterless narrowband photodetections in 2D layered perovskite single crystals. *Nat. Commun.* **10**, 806 (2019).

63. Li, S.-X. et al. Perovskite single-crystal microwire-array photodetectors with performance stability beyond 1 year. *Adv. Mater.* **32**, 2001998 (2020).

64. Zhao, Y. et al. Layered-Perovskite nanowires with long-range orientational order for ultrasensitive photodetectors. *Adv. Mater.* **32**, 1905298 (2020).

65. Zhang, Y., Liu, Y., Xu, Z., Yang, Z. & Liu, S. 2D Perovskite single crystals with suppressed ion migration for high-performance planar-type photodetectors. *Small* **16**, 2003145 (2020).

66. Liu, Y. et al. A 1300 mm^2 ultrahigh-performance digital imaging assembly using high-quality perovskite single crystals. *Adv. Mater.* **30**, 1707314 (2018).

67. Liu, Y. et al. Multi-inch single-crystalline perovskite membrane for high-detectivity flexible photosensors. *Nat. Commun.* **9**, 5302 (2018).

68. Yang, B. et al. Ultrasensitive and fast all-inorganic perovskite-based photodetector via fast carrier diffusion. *Adv. Mater.* **29**, 1703758 (2017).

Acknowledgements

Author contributions

K.Y. conceived the idea and designed the experiments. K.Y. and L.Shen supervised the project. Y.M. systematically contributed to the photodetector and photoelectronic measurements. L.Shan and Y.F. prepared samples and characterized their structural properties. Y.Y. conducted the DFT calculation. L.F. contributed to the XRD measurements of perovskite crystals. W.Z. and N.Y. assisted with the structural characterizations. H.H. assisted with the simulations and discussions. Y.L. and H.Z. contributed to discussions and assisted in the research. K.Y., Y.M., and L.Shen co-wrote the manuscript, and J.C. provided revisions. All authors discussed the results and commented on the manuscript.

Competing interests

The authors declare no competing interests.

Additional information

Supplementary information The online version contains supplementary material available at https://doi.org/10.1038/s41467-024-51762-3.

Correspondence and requests for materials should be addressed to Kai Yao.

Peer review information *Nature Communications* thanks René Janssen and the other anonymous reviewer(s) for their contribution to the peer review of this work. A peer review file is available.

Reprints and permissions information is available at http://www.nature.com/reprints

Publisher's note Springer Nature remains neutral with regard to jurisdictional claims in published maps and institutional affiliations.